1 # Emplacement age of the Sevier Gravity Slide, Utah, USA

2 Tiffany Rivera[1], McKenna Holliday[2], Brian Jicha[3], David H. Malone[4], Michael J. Braunagel[5], V.

3 Alex Bonilla Franco[6], Robert F. Biek[7], W. Ashley Griffith[8], David B. Hacker[9]

4 [1] Department of Geological Sciences, University of Missouri, Columbia, 65201, USA

5 [2] Department of Geological Sciences, University of Florida, Gainesville, 32603, USA

6 [3] Department of Geoscience, University of Wisconsin-Madison, Madison, 53706, USA

7 [4] Department of Geography, Geology and the Environment, Illinois State University, Normal, 61790, USA

8 [5] Department of Earth & Environmental Sciences, University of Minnesota Duluth, 55812

9 [6] Department of Geological Sciences, Jackson School of Geosciences, University of Texas, Austin, 78712, USA

10 [7] Utah Geological Survey, Salt Lake City, 84116, USA, retired

11 [8] School of Earth Sciences, Ohio State University, Columbus, 43210, USA

12 [9] Department of Geology, Kent State University, Kent, 44242, USA

13

14 *Correspondence to*: Tiffany A. Rivera (trivera@missouri.edu)

15

16

17

18

19

20

21

22

23

24

25   **Abstract.** The Marysvale volcanic field in southwestern Utah hosts three large volume gravity slides: the Sevier

26   (SGS), the Markagunt (MGS), and the Black Mountains (BGS). The gravity slides are composed of lahar deposits,

27   lava flows, and ash-flow tuffs erupted from former stratovolcanoes and other vents during the Oligocene and Miocene.

28   The ash-flow tuffs are prime targets for dating to constrain the age of the gravity slides because some ash-flow tuffs

29   are deformed within the slides, whereas others are undeformed and cap the slides. Furthermore, the gravity slides

30   produced pseudotachylyte during slide motion, a direct indicator for the timing of each slide. This work provides new

31   ^{40}Ar/^{39}Ar dates for several ash-flow tuffs and pseudotachylyte for the SGS, along with U/Pb zircon dates for one

32   deformed tuff and alluvium near the slide plane. Results show that the slide was emplaced at 25.25 ± 0.05 Ma and

33   was immediately followed by the eruption of the Antimony Tuff at 25.19 ± 0.02 Ma. The model presented here

34   suggests that the intrusion of magma related to the Antimony Tuff acted as a triggering mechanism for the slide, and

35   that slide movement itself led to decompression melting and eruption of the Antimony Tuff. This sequence of events

36   occurred on a geologically rapid timescale and may have been virtually instantaneous.

37

38   **Short summary.** The timing of an ancient gravity slide that originated in the Marysvale volcanic field (Utah, USA)

39   is constrained using ^{40}Ar/^{39}Ar dating of pseudotachylyte, a friction-induced glass that is generated during slide

40   movement, and the volcanic tuffs that were displaced by the slide and those that overly the slide mass. Our results

41   suggest that the Sevier gravity slide occurred at 25.25 Ma. The removal of such a large volume of material likely

42   allowed for the eruption of the Antimony Tuff at 25.19 Ma.

43   **1 Introduction**

44   Gravity slides are large volume mass movements that typically slide over shallowly dipping (≤ 3˚)

45   paleosurfaces. The Heart Mountain slide (Wyoming, USA) and the recently described Markagunt Gravity Slide

46   (Utah, USA) were coeval with volcanism and displaced km-thick sheets of volcanic rocks (Biek et al., 2022;

47   Malone, 1995; Malone et al., 2017). A characteristic feature of gravity slides is that they maintain the original

48   stratigraphy within the allochthonous sheets. The presence of volcanic materials offers opportunities to constrain the

49   emplacement age using several geochronological techniques. Furthermore, these megaslides are emplaced so rapidly

50   that they can generate pseudotachylyte, a friction induced melt hypothesized to have formed from the rocks involved

51   in sliding (Hacker 2017). Geochronology of the pseudotachylyte can directly constrain the age of the slide.

52   The Oligocene-Miocene Marysvale gravity slide complex (MGSC) in southwestern Utah (Fig. 1) is unique

53   in that it contains multiple, gigantic (1,700-2,000 km3; Hacker, 2017) individual gravity slides, including the Sevier

54   gravity slide (SGS), the 23 Ma Markagunt gravity slide (MGS; Holliday et al., 2022), and the Black Mountain

55   gravity slide (BGS) (Biek et al., 2019; 2022). Despite the coeval nature of the MGSC and the Marysvale volcanic

56   field (MVF), the causality of gravity slide emplacement is still unclear. Slide initiation may be due to magmatic

57   doming within the gravity slide's breakaway region, laccolith emplacement, or the accumulation of volcanic

58   material on weak strata may overload the crust and stimulate widespread slope failure (Hacker et al., 2018). Recent

59   work has improved the understanding about source material and kinematics of these landslides (Braunagel et al.,

60 2023; Hacker et al., 2023; Holliday et al., 2022; Zamanialavijeh et al., 2021). Notably, Holliday et al. (2022)

61 obtained $^{40}Ar/^{39}Ar$ dates on the ash-flow tuffs and pseudotachylyte from the MGS, then employed a novel Bayesian

62 statistical optimization age model to constrain an emplacement age. This work builds upon the previous

63 geochronology study of the MGS to determine the emplacement age of the SGS through $^{40}Ar/^{39}Ar$ dating of

64 pseudotachylyte formed during slide movement and of the bounding ash-flow tuffs. Our results unambiguously tie

65 pseudotachylyte formation to slide emplacement, affirming the catastrophic nature of the slides, while

66 simultaneously constraining the timing of slope failure relative to volcanic eruptions, which resolves outstanding

67 questions surrounding causality of gravity slides.

68 **2 Geologic background**

69   Early investigations in the MVF have provided the foundation for the discovery of the MGSC and

70 unraveling the associated stratigraphy as described in Biek et al. (2019). Geochemical investigations of the volcanic

71 units led to the identification of the calc-alkaline nature of the older rocks and younger bimodal basalts and high-

72 silica rhyolites (Rowley et al., 1975; Steven et al., 1977; Wender and Nash, 1979). Extensive mapping initiatives

73 were undertaken to unravel the geology, mineral resources, and economic potential of the region (e.g., Steven et al.,

74 1977; Cunningham and Steven, 1979; Steven et al., 1984; Palmer and Walton, 1990; Rowley et al., 1994; Rowley et

75 al., 1998; Granger and Bauer, 1950; Taylor et al., 1951; Kerr et al., 1957; among many others). This foundational

76 body of work contributes to understanding the spatial distribution of the volcanic centers and the stratigraphic

77 relationships between major eruptive units. The MVF straddles the boundary between the Colorado Plateau and the

78 Basin and Range province (Fig. 1) and covers >10,000 km^2, with an estimated total volume of 12,000 km^3 (Rowley

79 et al., 1998), and hosts three calderas: Three Creeks (~27 Ma), Monroe Peak (23–22 Ma), and Mount Belknap (22–

80 18 Ma). However, most of the eruptive products in the MVF have an unknown source, presumably because many

81 vent areas are now buried or overprinted by younger calderas. The breakaway regions for each gravity slide are

82 inferred to be entirely within the MVF (Biek et al., 2019, 2022), and suggest a genetic connection to local volcanic

83 activity. The breakaway zones of the SGS and MGS are overprinted by younger calderas (Biek et al., 2019, 2022),

84 and the breakaway of the BGS has presumably been eroded over the Mineral Mountains batholith (Biek 2022; Fig.

85 1).

86   Initiation of MVF volcanism is associated with Farallon slab rollback and southward migration of

87 volcanism across western North America. Peak volcanic activity (32–23 Ma) consisted of intermediate calc-alkaline

88 eruptions (Rowley et al., 1998; 2002) which account for ~90% of the MVF volcanic material contained in the

89 Bullion Canyon Volcanics and the Mount Dutton Formation (Rowley et al., 1994). The transition to bimodal basalt

90 and high-silica rhyolite volcanism occurred ca. 22 Ma and is linked to the transition from a subduction-style regime

91 to Basin and Range extension (Rowley et al., 1997). Basaltic eruptions have continued into the late Pleistocene

92 (Biek et al., 2015; Marchetti et al., 2020).

93   Recognition of the MGSC began with the early characterization of the Markagunt Megabreccia on the

94 Markagunt Plateau (Anderson, 1993). Described as isolated allochthonous masses (megabreccia), the Markagunt

95   Megabreccia consists of monolithic blocks and heterolithologic complexes as large as 2.5 km^2 and 50–200 m thick

96   (Sable and Maldonado, 1997). While these large masses were identified as gravity slides, they were interpreted to be

97   emplaced in several separate events from multiple sources (Anderson, 1993; Sable and Maldonado, 1997). However,

98   Hacker et al. (2014) and Biek et al. (2014; 2015) reinterpreted the Markagunt Megabreccia as part of a

99   catastrophically emplaced single slide mass based on new field evidence and mapping, and termed this the MGS.

100   The SGS was proposed in 2017 (Biek et al., 2017) and formally recognized in Biek et al. (2019). Along the western

101   flank of the SGS, Braunagel et al. (2023) characterized notable structural features that indicate intense deformation,

102   clastic dikes of basal material into overlying rocks, pseudotachylyte, and cataclastic basal zones. Loffer (2024)

103   identified several pseudotachylyte sites within the SGS, and proposed an SGS maximum depositional age of 25.5

104   Ma using detrital zircon extracted from the basal layer of the slide in two locations.

105
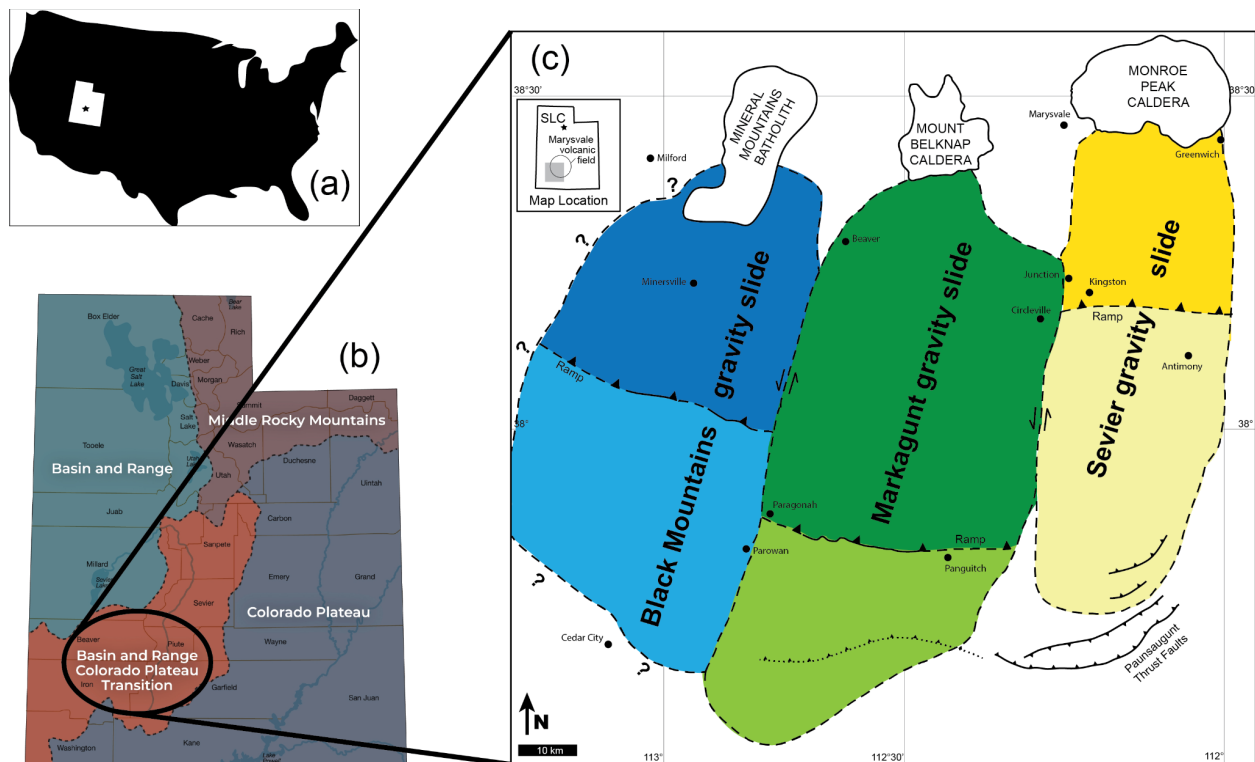
Figure 1: Regional maps of study location. (a) The state of Utah within the United States. (b) Physiographic provinces of Utah, highlighting the Basin and Range to Colorado transition zone. Figure modified from the Utah Geological Survey website (https://geology.utah.gov/popular/utah-landforms/). (c) Markagunt gravity slide complex within the Marysvale volcanic field (shown in inset). Note locations of three gravity slides, each represented by a different color. The breakaway areas (dark colors) for the Sevier and Markagunt slides are overprinted by the calderas of the Marysvale volcanic field. The breakaway region of the Black Mountains gravity slide has been eroded due to the uplift of the Mineral Mountains batholith. Lighter shades represent the runout of the gravity slide. Figure modified from (Braunagel et al., 2023).
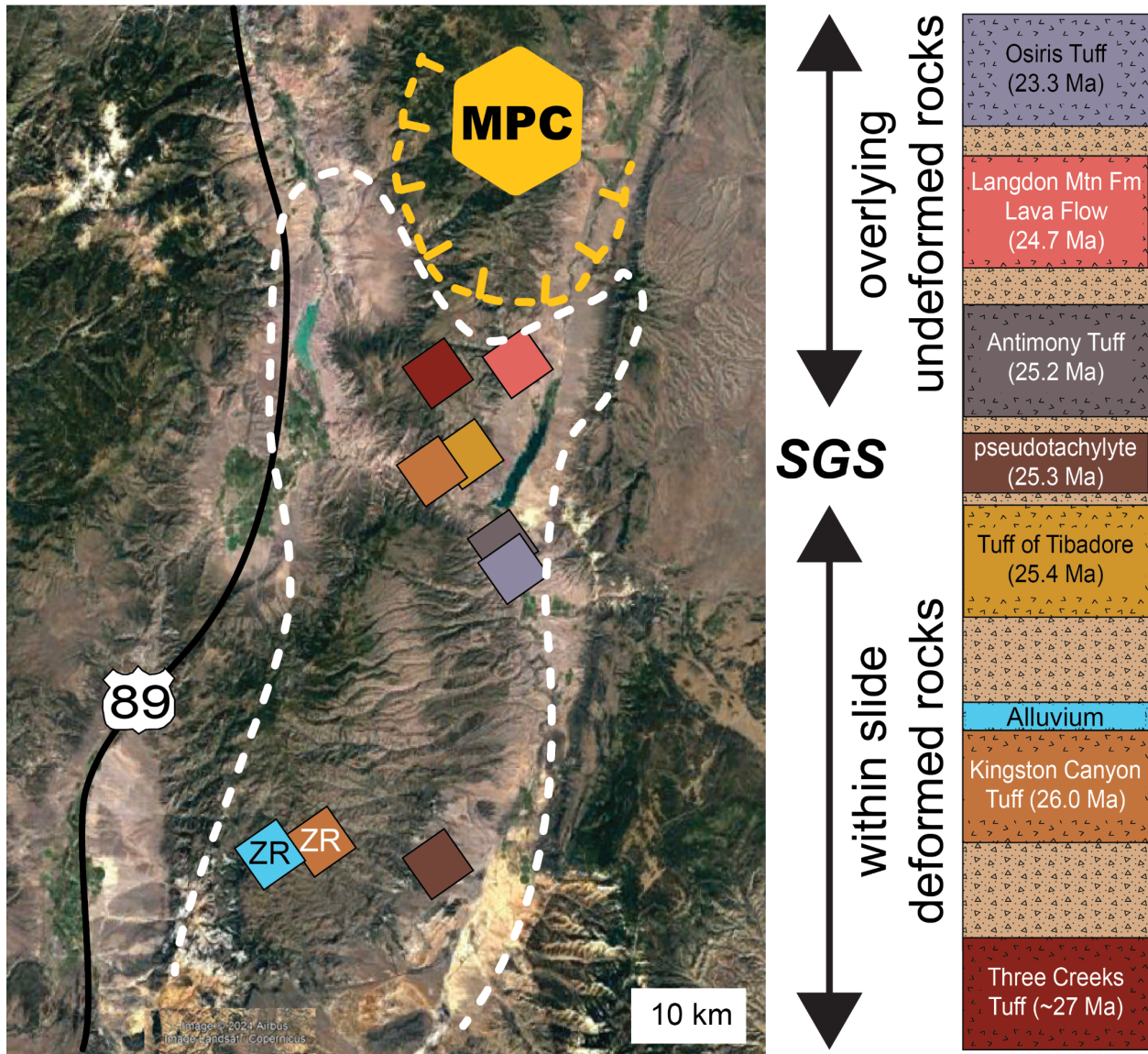
Figure 2: Sevier gravity slide location (white boundary) shown with Monroe Peak Caldera (MPC) and sampling locations. To the right, a simplified stratigraphic section (not to scale) of the Mount Dutton Formation (light brown) with interspersed ash-flow tuffs and other rocks investigated in this study. The allochthonous block of the SGS includes the within slide deformed ash-flow tuffs and pseudotachylyte, whereas the overlying undeformed ash-flow tuffs post-date slide emplacement. Locations labeled with "ZR" indicate samples collected for zircon U/Pb dating. © Google Earth, using 2024 imagery of Airbus, Landsat, Conpernicus.

3 Materials and methods

The units investigated here are grouped by their stratigraphic position relative to the SGS. Ash-flow tuffs 'within' the slide material are deformed and were displaced by slide motion as an allochthonous block. Ash-flow tuffs 'above' the slide are all undeformed by and postdate the SGS (Fig. 2). The Kingston Canyon Tuff (samples 21MGSC-02 and KCT; Fig. 3a-c) is a densely welded, red-purple, lithic tuff. Plagioclase is the major mineral phase,

128 with minor hornblende and biotite (Fig. 3c). Lithic components consist of mafic igneous rocks (Fig. 3b). A sample

129 of the alluvial facies of the Mt. Dutton Formation overlying the KCT sample was collected to examine the detrital

130 zircon record (MVC6-21-10-16-2). The tuff of Tibadore (21MGSC-01, Fig. 3d-f) is a crystal poor, densely welded

131 lithic ash-flow tuff. Fresh surfaces are purple with black fiamme 1–3 cm long (Fig. 3e) The Antimony Tuff

132 (PH030218-1, Fig. 3i) is a densely welded, relatively crystal-poor ash-flow tuff, with a red groundmass containing

133 large plagioclase, minor pyroxene, and lithics. The Langdon Mountain Formation contains a lower lahar facies and

134 an upper lava flow facies; only the lava flow facies, dated here, clearly postdates the SGS (Rowley et al., 2002). The

135 lava flow facies is described as a dacitic lava flow containing large phenocrysts of plagioclase, hornblende, and

136 minor pyroxene and considered the last of the minor eruptive sequences prior to the eruption of the caldera-forming

137 Osiris Tuff (Rowley et al., 1994); eruptive vents of the Langdon Mountain rocks were likely destroyed by

138 emplacement of the Monroe Peak caldera. The Osiris Tuff (PH030218-2) contains dominantly large feldspar

139 phenocrysts, conspicuous biotite, and minor pyroxene within a gray groundmass. The Osiris Tuff is not deformed by

140 the SGS, but was deformed by the later 23 Ma MGS emplacement near the breakaway zone (Biek et al., 2019;

141 Holliday et al., 2022). Pseudotachylyte (24MSGC-37, Fig. 3g-h) is found on shear planes and in injection veins as

142 much as 200 m above the basal slip surface.

143
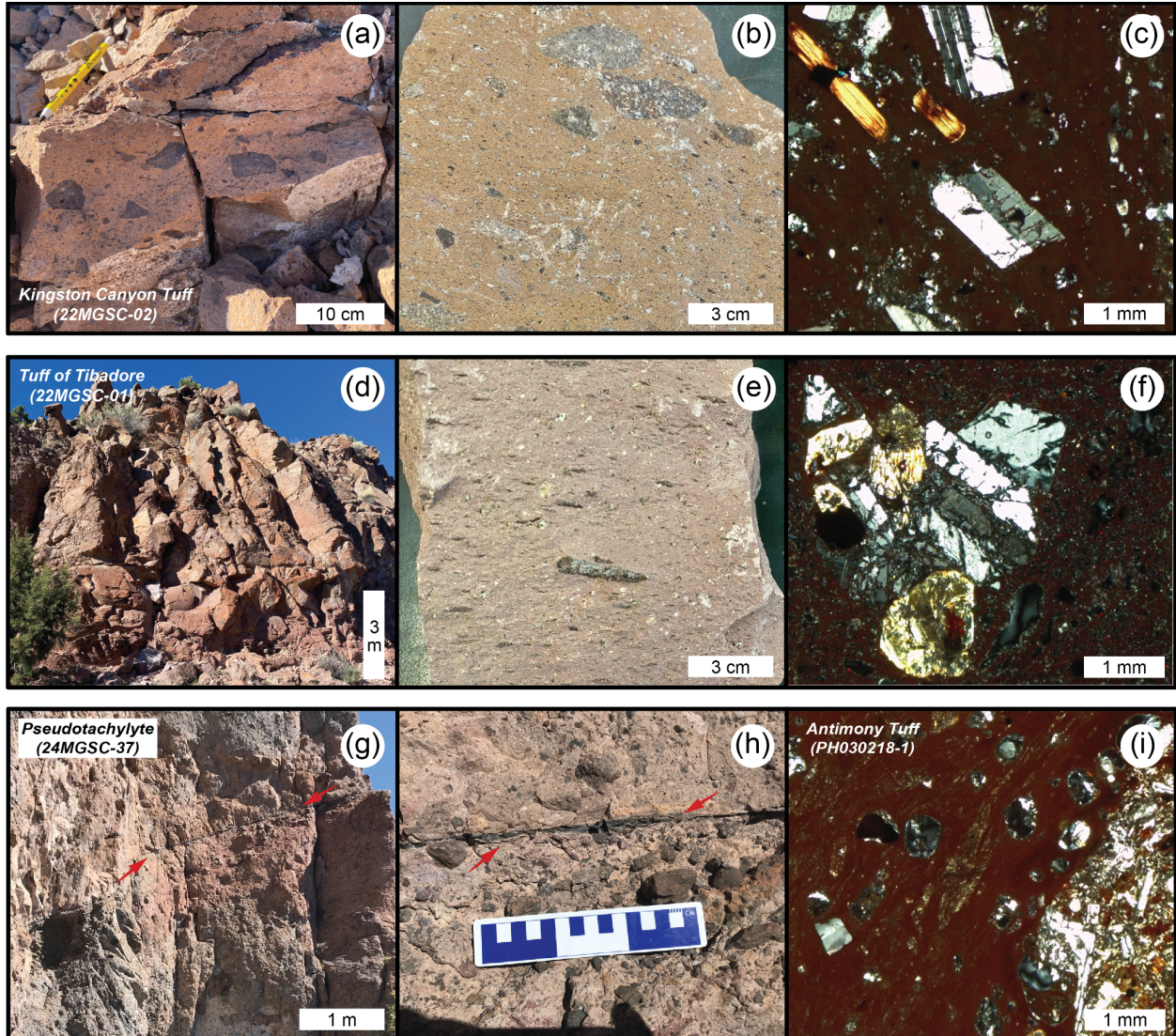
Figure 3: (a) Outcrop of Kingston Canyon Tuff; (b) Hand sample of Kingston Canyon Tuff showing abundant lithic fragments; (c) thin section of Kingston Canyon Tuff showing plagioclase and biotite phenocrysts; (d) outcrop of tuff of Tibadore; (e) tuff of Tibadore hand sample with prominent fiamme; (f) thin section of the tuff of Tibadore showing rare crystal clot; (g) outcrop of pseudotachylyte vein; (h) outcrop of pseudotachylyte vein; (i) thin section of Antimony Tuff showing mafic xenolith (right side of image) and fiamme. Thin section photographs were taken in crossed polarized light.

3.1 ^{40}Ar/^{39}Ar analysis

Samples of each ash-flow tuff, lava flow, and pseudotachylyte described above were processed by standard crushing, magnetic, and density techniques, then sieved at 180-350 μm to prepare for ^{40}Ar/^{39}Ar analysis. Under a binocular microscope, handpicked sanidine was extracted from the Osiris and Antimony Tuffs, and plagioclase was selected from the tuff of Tibadore, Kingston Canyon Tuff, and Langdon Mountain lava flow. Pseudotachylyte glass was also handpicked prior to analysis. Selected materials were co-irradiated with the 28.201 Ma Fish Canyon Tuff

157   sanidine neutron fluence monitor (Kuiper et al., 2008) at the Cd-lined facility at the Oregon State University TRIGA

158   reactor. Single crystal total fusion analyses were conducted for the ash-flow tuffs whereas incremental heating

159   experiments were conducted for purified bulk samples of the lava flow and pseudotachylyte. All analyses were

160   performed at the WiscAr Geochronology Lab, University of Wisconsin-Madison using either the Noblesse 5

161   Collector (Jicha et al., 2016) or the Isotopx NGX-600 mass spectrometers (Mixon et al., 2022).

162   **3.2 Zircon U/Pb analysis**

163   Zircon crystals were extracted by traditional methods of crushing and grinding, followed by separation by

164   panning, heavy liquids, and a Frantz magnetic separator. A large split of grains is incorporated into a 1" epoxy

165   mount together with fragments or loose grains of Sri Lanka, FC-1, and R33 zircon crystals that are used as primary

166   standards. The mounts are sanded down to a depth of ~20 microns, polished, imaged, and cleaned prior to isotopic

167   analysis. Grains of interest are imaged to provide a guide for locating analysis pits in optimal locations, and to aid in

168   interpreting results. BSE images were generated with a Hitachi 3400N SEM and a Gatan CL2 detector system

169   (supplementary materials). U/Pb geochronologic analyses were conducted by laser ablation inductively coupled

170   plasma mass spectrometry (LA-ICPMS) at the Arizona LaserChron Center (www.laserchron.org). Methods for U/Pb

171   geochronology have been described by Gehrels et al. (2006, 2008), Gehrels and Pecha (2014), Pullen et al. (2018),

172   and Sundell et al. (2021).

173   **4 Results**

174   **4.1 ^{40}Ar/^{39}Ar geochronology**

175   Thirty-three plagioclase crystals from the Kingston Canyon Tuff (21MGSC-02) generated a range of

176   radiogenic yields. As such, only the seven grains with >70% ^{40}Ar* were used to calculate the weighted mean and

177   associated statistics. The seven grains yield ages from 25.88 ± 0.06 Ma to 26.08 ± 0.08 Ma and produce a weighted

178   mean of 25.97 ± 0.05 Ma (n = 7/33; MSWD = 1.27; p = 0.37; Fig. 4). All uncertainties reported in this work include

179   errors associated with the irradiation parameter, J. Nine single crystal plagioclase fusion analyses from the tuff of

180   Tibadore (21MGSC-01) yielded dates from 25.33 ± 0.01 Ma to 25.91 ± 0.08 Ma. However, in order to filter the data

181   in a consistent manner, analyses with <70% ^{40}Ar* were omitted from calculations. Thus a weighted mean for five of

182   the analyses is 25.43 ± 0.04 Ma (MSWD = 0.74; p = 0.40; Fig. 4). Incremental heating of pseudotachylyte glass

183   (24MGSC-37) produced a plateau age of 25.25 ± 0.06 Ma (MSWD = 0.60; p = 0.90; Fig. 5a) including >85% of the

184   cumulative ^{39}Ar$_K$. The ^{40}Ar/^{36}Ar isochron intercept of 292.4 ± 8.8 is within uncertainty of the atmospheric value

185   (Lee et al., 2006). Two locations were sampled for Antimony Tuff and sanidine from both were analyzed by total

186   fusion. Thirteen grains from sample PH030218-1 produced dates ranging from 25.02 ± 0.07 Ma to 25.26 ± 0.07 Ma.

187   A weighted mean of these yields an age of 25.14 ± 0.06 Ma (MSWD = 1.33; p = 0.25). Twenty-seven sanidine

188   grains from sample (MP071020-2) produced dates ranging from 25.14 ± 0.03 Ma to 25.23 ± 0.03 Ma, and a

189   weighted mean of these produce an age of 25.19 ± 0.02 Ma (MSWD = 1.45; p = 0.08). Combining the two datasets

190 and applying normalized Median Absolute Deviation (nMAD) filter of 1.5 (e.g., Kuiper et al., 2008), 35 of the 40

191 total grains produce a weighted mean age of 25.19 ± 0.02 Ma (MSWD = 1.17; p = 0.26; Fig. 4). Bulk plagioclase

192 from the Langdon Mountain lava flow was incrementally heated and produced a plateau age of 24.68 ± 0.32 Ma

193 (MSWD = 0.71; p = 0.82; Fig. 5b) with 100% of the cumulative $^{39}Ar_K$. The $^{40}Ar/^{36}Ar$ isochron intercept of 299.3 ±

194 10.3 is within uncertainty of the atmospheric value (Lee et al., 2006). Holliday et al. (2022) report total fusion dates

195 of thirteen sanidine grains from the Osiris Tuff, which produced dates ranging from 23.16 ± 0.08 Ma to 23.37 ± 0.04

196 Ma and a weighted mean age of 23.27 ± 0.05 Ma (MSWD = 1.60; p = 0.12).

197
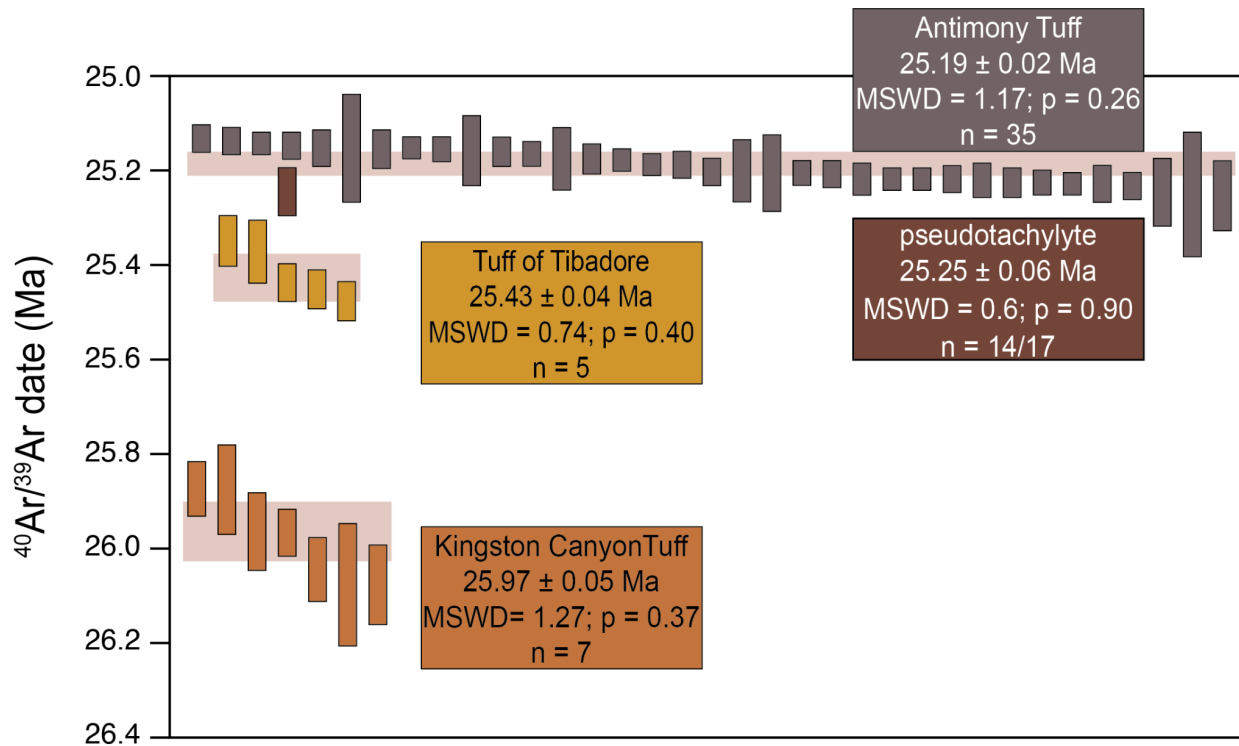
198
199 **Figure 4: Results of single crystal fusion $^{40}Ar/^{39}Ar$ analyses for the volcanic units overlying and within the Sevier gravity**
200 **slide, and incremental heating result of the slide-generated pseudotachylyte. Height of each bar represents the $^{40}Ar/^{39}Ar$**
201 **date and 2σ uncertainty of a single experiment. The height of the shaded region behind Kingston Canyon Tuff, tuff of**
202 **Tibadore, and Antimony Tuff represents the weighted mean with 2σ uncertainty of the shown analyses. n = number of**
203 **single crystal analyses used to calculate the weighted mean, except for the pseudotachylyte, in which n refers to the number**
204 **of incremental heating steps used to calculate a plateau age.**

205
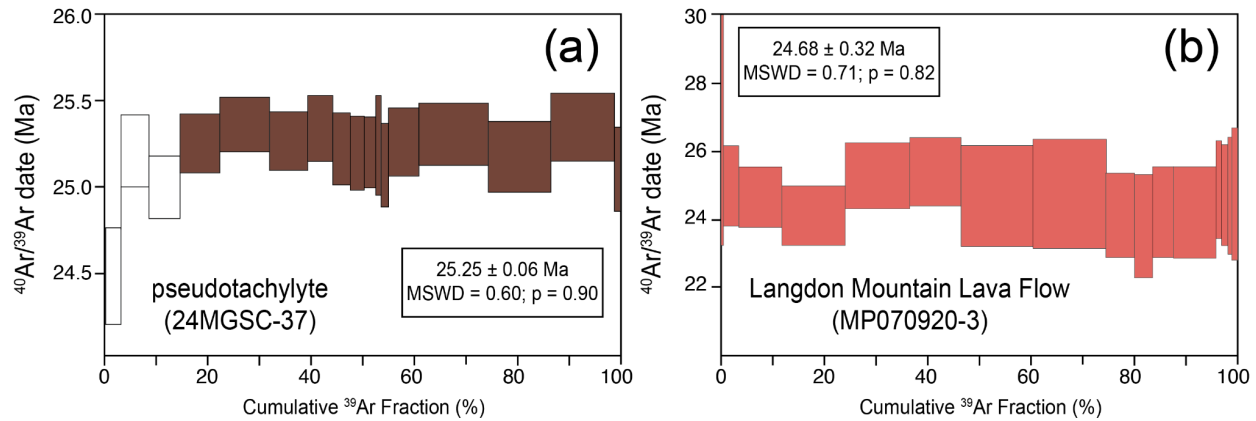
Figure 5: Results of ^{40}Ar/^{39}Ar incremental heating analyses for a lava flow and pseudotachylyte investigated in this work. (a) Incremental heating results of the pseudotachylyte. Each box height represents the date ± 2σ. Filled incremental heating steps were used in calculations; unfilled steps were omitted. (b) Incremental heating results of the Langdon Mountain Lava Flow. Each box height represents the date ± 2σ. All incremental heating steps were used in calculations.

4.2 Zircon U/Pb geochronology

Zircon ^{206}Pb/^{238}U dates from the Kingston Canyon Tuff (sample KCT) range from 25.11 ± 0.37 Ma to 1871 ± 12 Ma (n = 122; supplementary materials). Precambrian grains (n = 5) and the single young zircon (n = 1) that is outside statistical uncertainty of the ^{40}Ar/^{39}Ar eruption age were excluded from calculations. The ^{206}Pb/^{238}U dates produce a bimodal distribution (Fig. 6), with mixture model deconvolution peaks at 26.41 ± 0.06 Ma (29%) and 33.96 ± 0.05 Ma (54%) (Sambridge 1994; Ludwig, 2012). Zircon from the Mount Dutton Formation produced ^{206}Pb/^{238}U dates ranging from 25.13 ± 0.50 Ma to 1823 ± 15 Ma (n = 156). Grains older than 50 Ma were excluded from calculations (n = 17). The ^{206}Pb/^{238}U dates of the Mount Dutton Formation produce a fairly unimodal distribution, with a tail to slightly older (>30 Ma) dates. Mixture modeling deconvolution suggests the dominant population is 26.56 ± 0.04 Ma (78%). However, this value is skewed slightly older than the age of the peak (Fig. 6).

The maximum depositional age (MDA) was estimated using maximum likelihood age algorithms (MLA; Galbraith and Laslett, 1993; Vermeesch, 2021). The MLA age for the Kingston Canyon Tuff of 26.13 ± 0.20 Ma (Fig. 7a) is in agreement with the ^{40}Ar/^{39}Ar eruption age, but is significantly younger than the mixture modeling deconvolution age discussed above. The MLA for the alluvium of the Mount Dutton Formation is 25.24 ± 0.17 Ma (Fig. 7b), again significantly younger than the deconvolution age.
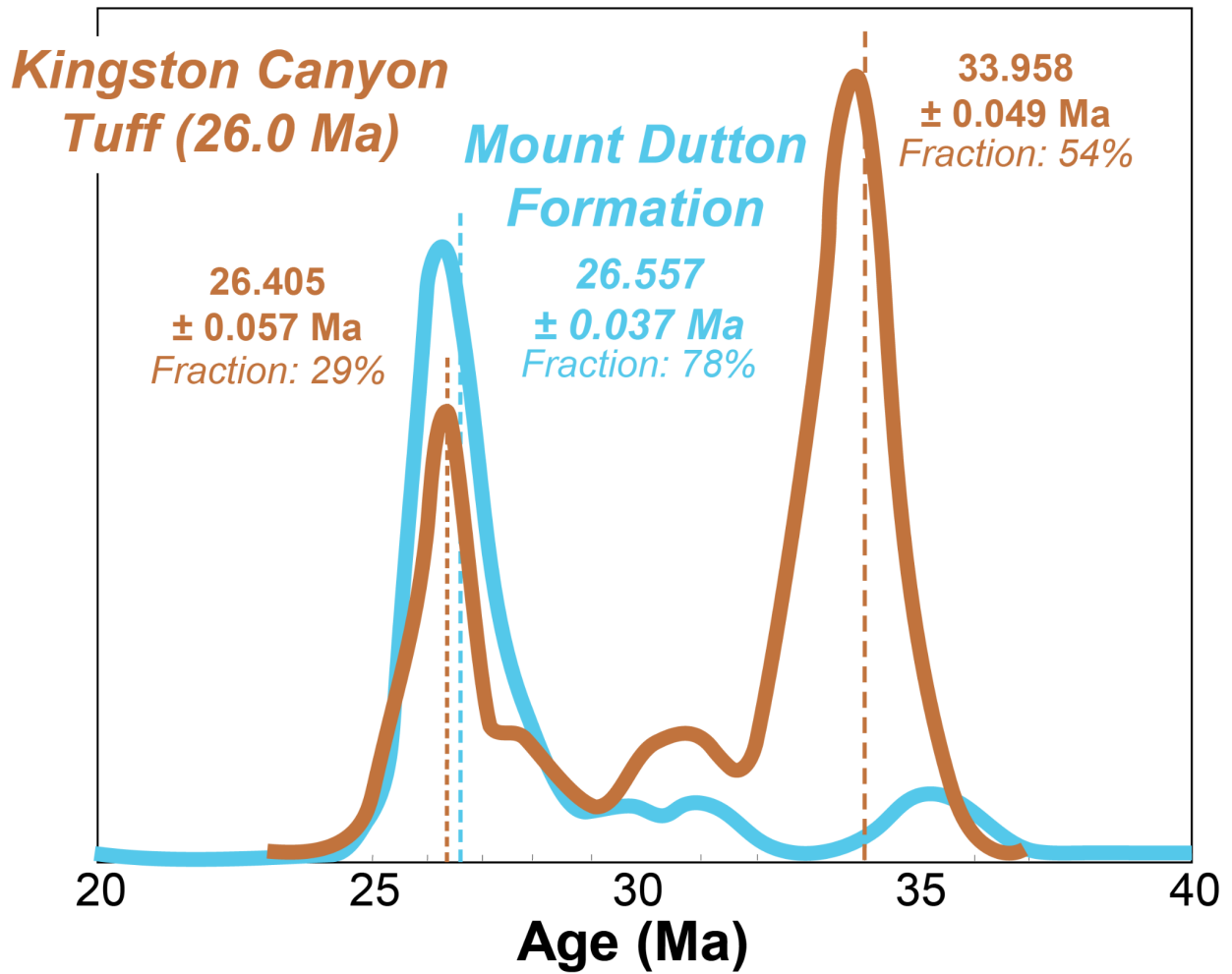
Figure 6: Probability distribution functions for U/Pb zircon dates from the Kingston Canyon Tuff (sample KCT) and overlying alluvium of the Mount Dutton Formation. Mixture modeling deconvolution ages and fraction of total grains are displayed for each mode. The dashed lines mark those deconvolution ages relative to the probability distribution functions.

Kingston Canyon Tuff

(a)

MLA: 26.13 ± 0.20 Ma

Mount Dutton Formation

(b)

MLA: 25.24 ± 0.17 Ma
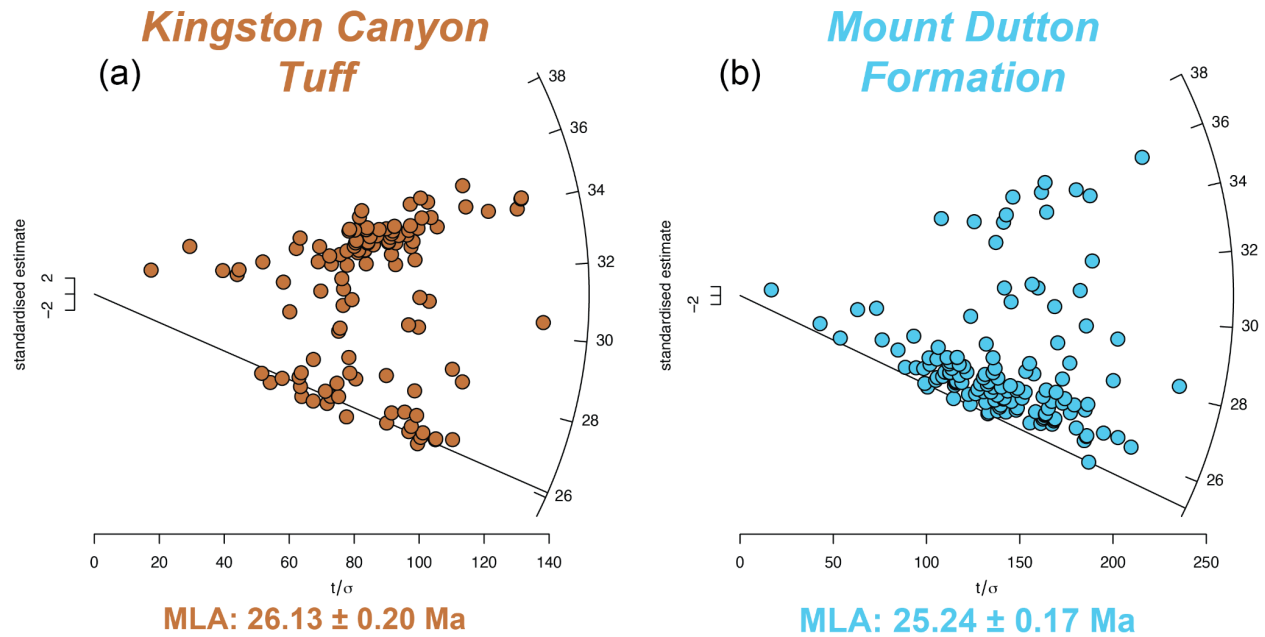
Figure 7: Radial plots of zircon U/Pb age data for the (a) Kingston Canyon Tuff and (b) overlying alluvium of the Mount Dutton Formation. MLA: Maximum Likelihood Age. Plots generated using IsoplotR with the algorithms of Galbraith and Laslett (1993) and Vermeesch (2021) and a logarithmic transformation.

5 Discussion

Emplacement of the SGS was previously constrained to between 23.0 and 25.4 Ma based on a K-Ar age 25.4 ± 0.9 Ma for the tuff of Tibadore, which is the youngest deformed volcanic unit in the SGS, and the 23.0 Ma age of the overlying, undeformed Osiris Tuff (Biek et al., 2019). This age was updated to between 26.2 and 25.1 Ma based on an age of 25.1 Ma for the Antimony Tuff, which post-dates emplacement, and an age of 26.2 Ma for the Buckskin Breccia, the youngest rocks underlying the SGS (Rowley et al., 1994). The breccia itself had not been dated, but included clasts of the Spry and Showalter quartz monzonite intrusions which have similar intrusion dates (Biek et al., 2022). Loffer (2024) estimated an emplacement age of 25.5 Ma based on detrital zircon U/Pb dates from the basal layer of the SGS at two locations. The discovery of pseudotachylyte within the SGS offered an additional opportunity to refine the emplacement age; this work presents an ^{40}Ar/^{39}Ar age of 25.25 ± 0.05 Ma for SGS emplacement, consistent with previous estimates but with higher precision. The significant improvement in the plateau age uncertainty for the SGS experiment relative to the pseudotachylyte analysis of Holliday et al. (2022) is because the analyses were performed using the NGX-600 mass spectrometer, which has stable ATONA®-backed Faraday collectors (Mixon et al. 2022) and an incredibly low noise floor (Cox et al., 2020). As such a Bayesian statistical optimization age is not needed. Emplacement occurred approximately 170 kyr after the eruption of the tuff of Tibadore and immediately preceding the eruption of the Antimony Tuff. The slide may have occurred up to 130

253   kyr prior to the eruption of the Antimony Tuff, or may have occurred near simultaneously, given that the ages and

254   uncertainties for the pseudotachylyte and Antimony Tuff are statistically indistinguishable. Importantly, because the

255   pseudotachylyte had been found within the upper plate associated with subsidiary faults, it has been impossible,

256   until now, to conclusively demonstrate it was formed during slide emplacement. The pseudotachylyte age reported

257   here thus provides tight constraints on the timing of SGS emplacement, and confirms the catastrophic nature of

258   emplacement, consistent with prior interpretations (e.g., Biek et al., 2019; Braunagel et al., 2023). The Langdon

259   Mountain lava flow, dated at 24.7 Ma, represents the last minor eruptive sequence prior to the formation of the 23.0

260   Ma caldera by the eruption of the Osiris Tuff. The age of the Langdon Mountain lava flow is consistent with

261   stratigraphic observations, but does not contribute to better understanding the timing of the SGS.

262   The bimodal zircon U/Pb distribution of the Kingston Canyon Tuff suggests a significant zircon

263   contribution from a previously crystallized subsurface magma. Xenocrystic inheritance is not observed in the

264     $^{40}Ar/^{39}Ar$ data, possibly due to the small number of grains analyzed. Interestingly, the U/Pb zircon record of the

265   alluvium atop the Kingston Canyon Tuff does not contain a strong 34 Ma signal. This, along with the overall

266   younger MLA of the Mount Dutton alluvium, suggests that the dominant sediment input was derived from a

267   different source. The Eocene Heart Mountain gravity slide in Wyoming is a comparable feature that is associated

268   with igneous activity of the Absaroka volcanic field. Initiation of the gravity slide has been debated, ranging from

269   incremental movement spanning millions of years (Malone et al. 2014), or catastrophic emplacement spanning

270   several minutes to hours (Craddock et al. 2009). Recently, a lamprophyre suite (breccia, dike, diatreme) was

271   identified at the base of allochthonous rocks. High-precision zircon U/Pb dating of the lamprophyre yielded dates

272   that were identical to those obtained from other basalt cataclasites, leading to the interpretation that the eruption of

273   the diatreme triggered the gravity slide (Malone et al., 2017).

274   In both the MGSC and Heart Mountain, trigger mechanisms for gravity slides have been poorly

275   understood; however, timing of igneous events relative to the sliding are essential for unraveling the relationship

276   between the two types of events. In the Eocene Heart Mountain gravity slide, igneous activity apparently led to

277   sliding, whereas in the Oligocene SGS, decompression associated with the gravity slide may have initiated the

278   eruption of the Antimony Tuff. However, the timing of the intrusion of the magma body which became the

279   Antimony Tuff is still unknown. Additional insights into the processes associated with Antimony Tuff's pre-

280   eruption magma injection into the upper crust could be unraveled using detailed mineral analyses.

281   **6 Conclusion**

282   New high-precision $^{40}Ar/^{39}Ar$ dating of key units involved in the SGS suggest an emplacement age of 25.25

283   Ma ± 0.05 Ma. This is approximately two million years prior to the Markagunt gravity slide (Holliday et al., 2022).

284   The emplacement model proposed here is that the slide was initiated from injection of magma, which led to slope

285   failure. This prompted decompression and ultimately the eruption of the 25.19 ± 0.02 Ma Antimony Tuff. The

286   association of magmatic intrusions and gravity slides was also proposed at Heart Mountain, Wyoming, suggesting

287   that large-volume volcanic plateaus may generate these types of catastrophic events more frequently than previously

288 identified. Further, we begin to resolve the questions about causes for gravity slides (Hacker, 2014) and assess the

289 relationship between igneous activity and mass movements.

290

291 **Data availability**. All data used in this work are provided in the supplementary materials.

292

293 **Supplementary materials**. The supplement is available online.

294

295 **Author contributions**. TR and MH designed the study and performed field collection with BJ, DHM, MJB, RFB,

296 and WAG. BJ and BHM performed ^{40}Ar/^{39}Ar and U/Pb data collection, respectively. TR, MH, and VABF

297 performed data analysis. TR prepared the figures and the manuscript, and all authors contributed to the interpretation

298 of results and improvement of the manuscript.

299

300 **Competing interests**. The authors declare no competing interests.

301

309

310

311

312 **References**

313 Anderson, J.J., 1993. The Markagunt megabreccia : large Miocene gravity slides mantling the northern Markagunt

314 Plateau, southwestern Utah. Utah Geological Survey, Miscellaneous Publication 93-2. https://doi.org/10.34191/mp-

315 93-2

316 Biek, R.F, Hacker, D.B., Rowley, P.D., 2014. New constraints on the extent, age, and emplacement history of the

317 early Miocene Markagunt Megabreccia, southwest Utah—the deposit of one of the world's largest subaerial gravity

318 slides, Geology of Utah's far south 43, 565–598.

319 Biek, R.F., Hacker, D.B., Rowley, P.D., 2017. Catastrophic mega-scale landslide failure of large volcanic fields.

320 Thompson Field Forum. https://doi.org/10.1130/abs/2018rm-314106

321

322   Biek, R.F., Rowley, P.D., Anderson, J.J., Maldonado, F., Moore, D.W., Hacker, D.B., Eaton, J.G., Hereford, R.,

323   Sable, E.G., Filkorn, H.F., Matyjasik, B., 2015. Geologic map of the Panguitch 30' x 60' quadrangle, Garfield, Iron,

324   and Kane counties, Utah.

325

326   Biek, R.F., Rowley, P.D., Hacker, D.B., 2022. Utah's ancient mega-landslides—geology, discovery, and guide to

327   Earth's largest terrestrial landslides. Utah Geological Survey Circular 132. https://doi.org/10.34191/c-132

328

329   Biek, R.F., Rowley, P.D., Hacker, D.B., 2019. The Gigantic Markagunt and Sevier Gravity Slides Resulting from

330   Mid-Cenozoic Catastrophic Mega-Scale Failure of the Marysvale Volcanic Field, Utah, USA. Thompson Field

331   Forums.

332

333   Braunagel, M.J., Griffith, W.A., Biek, R.F., Hacker, D.B., Rowley, P.D., Malone, D.H., Mayback, D., Rivera, T.A.,

334   Loffer, Z., Smith, Z.D., 2023. Structural Relationships Across the Sevier Gravity Slide of Southwest Utah and

335   Implications for Catastrophic Translation and Emplacement Processes of Long Runout Landslides. Geochemistry

336   Geophysics Geosystems 24. https://doi.org/10.1029/2022gc010783

337

338   Cox, S.E., Hemming, S.R., Tootell, D., 2020. The Isotopx NGX and ATONA Faraday amplifiers: Geochronology 2,

339   231–243, https://doi .org /10 .5194 /gchron-2-231-2020.

340

341   Craddock, J.P., Malone, D.H., Magloughlin, J., Cook, A.L., Rieser, M.E. Doyle, J.R., 2009. Dynamics of the

342   emplacement of the Heart Mountain allochthon at White Mountain: Constraints from calcite twinning strains,

343   anisotropy of magnetic susceptibility, and thermodynamic calculations. Geological Society of America Bulletin 121,

344   919-938.

345

346   Cunningham, C.G., Steven, T.A., 1979. Mount Belknap and Red Hills calderas and associated rocks, Marysvale

347   volcanic field, west-central Utah, USGS Numbered Series 1468.

348

349   Gailbraith, R.F., Laslett, G.M., 1993. Statistical models for mixed fission track ages. Nuclear Tracks and Radiation

350   Measurements 21, 459-470. https://doi.org/10.1016/1359-0189(93)90185-C.

351

352   Gehrels, G.E., Pecha, M., 2014. Detrital zircon U-Pb geochronology and Hf isotope geochemistry of Paleozoic and

353   Triassic passive margin strata of western North America. Geosphere 10, 49–65, DOI:10.1130/geos.s.12187251.v1.

354

355   Gehrels, G.E., Valencia, V., Pullen, A., 2006. Detrital zircon geochronology by laser-ablation multicollector ICPMS

356   at the Arizona LaserChron Center. The Paleontological Society Papers 12, 67–76,

357   DOI:10.1017/s1089332600001352.

358

359   Gehrels, G.E., Valencia, V., Ruiz, J., 2008. Enhanced precision, accuracy, efficiency, and spatial resolution of U-Pb
360   ages by laser ablation-multicollector-inductively coupled plasma-mass spectrometry. Geochemistry Geophysics
361   Geosystems 9, DOI:10.1029/2007gc001805.
362
363   Granger, H.C., Bauer, H.L., 1950. Preliminary examination of uranium deposits near Marysvale, Piute County, Utah
364   (No. 33). US Geological Survey.
365
366   Hacker, D., Biek, R.F., Rowley, P., Griffith, W.A., Malone, D., Rivera, T., 2023. Catastrophic gravity sliding of the
367   Marysvale volcanic field during rapid growth of laccolithic batholiths: insights from the Cenozoic Marysvale gravity
368   slide complex, southwest Utah. https://doi.org/10.1130/abs/2023am-394566
369
370   Hacker, D.B., Biek, R.F., Rowley, P.D., 2014. Catastrophic emplacement of the gigantic Markagunt gravity slide,
371   southwest Utah (USA): Implications for hazards associated with sector collapse of volcanic fields. Geology 42, 943–
372   946. https://doi.org/10.1130/g35896.1
373
374   Hacker, D.B., Rowley, P.D., Biek, R.F., 2018. Catastrophic collapse features in volcanic terrains: styles and links to
375   subvolcanic magma systems. In: Advances in Volcanology. Springer. https://doi.org/10.1007/11157_2017_1001
376
377   Holliday, M.E., Rivera, T., Jicha, B., Trayler, R.B., Biek, R.F., Braunagel, M.J., Griffith, W.A., Hacker, D.B.,
378   Malone, D.H., Mayback, D.F., 2022. Emplacement age of the Markagunt gravity slide in southwestern Utah, USA.
379   Terra Nova. https://doi.org/10.1111/ter.12630
380
381   Jicha, B.R., Singer, B.S., Sobol, P., 2016. Re-evaluation of the ages of 40Ar/39Ar sanidine standards and
382   supereruptions in the western U.S. using a Noblesse multi-collector mass spectrometer. Chemical Geology 431, 54–
383   66. https://doi.org/10.1016/j.chemgeo.2016.03.024
384
385   Kerr, P.F., Brophy, G.P., Dahl, H.M., Green, J., Woolard, L.E., 1957. Marysvale, Utah, Uranium Area: Geology,
386   Volcanic Relations, and Hydrothermal Alteration, Marysvale, Utah, Uranium Area: Geology, Volcanic Relations,
387   and Hydrothermal Alteration (Paul F. Kerr, Gerald P. Brophy, Harry M. Dahl, Jack Green, and Louis E. Woolard,
388   eds.), Geological Society of America 64.
389
390   Kuiper, K.F., Deino, A., Hilgen, F.J., Krijgsman, W., Renne, P.R., Wijbrans, J.R., 2008. Synchronizing Rock Clocks
391   of Earth History. Science 320, 500–504. https://doi.org/10.1126/science.1154339
392
393   Lee, J.-Y., Marti, K., Severinghaus, J.P., Kawamura, K., Yoo, H.-S., Lee, J.B., Kim, J.S., 2006. A redetermination
394   of the isotopic abundances of atmospheric Ar. Geochimica et Cosmochimica Acta 70, 4507–4512.
395   https://doi.org/10.1016/j.gca.2006.06.1563

396

397 Loffer, Z.J., Hacker, D.B., Malone, D.H., Biek, R.F., d Rowley, P. D., 2020, Zircon geochronology of the basal

398 layer of the Sevier gravity slide, Marysvale volcanic field, Utah, USA. Geological Society of America Abstracts

399 with Programs 52, doi: 10.1130/abs/2020RM-346702.

400

401 Ludwig, K. R., 2012. User's manual for Isoplot version 3.75–4.15: a geochronological toolkit for Microsoft Excel.

402 Berkeley Geochronological Center Special Publication 5.

403

404 Malone, D.H., 1995. Very large debris-avalanche deposit within the Eocene volcanic succession of the northeastern

405 Absaroka Range, Wyoming. Geology 23, 661–664. https://doi.org/10.1130/0091-

406 7613(1995)023<0661:vldadw>2.3.co;2

407

408 Malone, D.H., Craddock, J.P., Anders, M.H., Wulff, A.P., 2014. Constraints on the emplacement age of the massive

409 Heart Mountain Slide, Northwestern Wyoming. Journal of Geology 122, 671-685. DOI:10.1086/678279

410

411 Malone, D.H., Craddock, J.P., Schmitz, M.D., Kenderes, S., Kraushaar, B., Murphey, C.J., Nielsen, S., Mitchell,

412 T.M., 2017. Volcanic Initiation of the Eocene Heart Mountain Slide, Wyoming, USA. Journal of Geology 125, 439–

413 457. https://doi.org/10.1086/692328

414

415 Marchetti, D.W., Stork, A.L., Solomon, D.K., Cerling, T.E., Mace, W., 2020. Cosmogenic 3He exposure ages of

416 basaltic flows from Miller Knoll, Panguitch Lake, Utah: Using the alternative isochron approach to overcome low-

417 gas crushes. Quaternary Geochronology 55, 101035. https://doi.org/10.1016/j.quageo.2019.101035

418

419 Mixon, E. E., Jicha, B. R., Tootell, D., Singer, B.S., 2022. Optimizing 40Ar/39Ar analyses using an Isotopx NGX-

420 600 mass spectrometer. Chemical Geology 593, 120753. https://doi.org/10.1016/j.chemgeo.2022.120753

421

422 Palmer, B.A., Walton, A.W., 1990. Accumulation of volcaniclastic aprons in the Mount Dutton Formation

423 (Oligocene-Miocene), Marysvale volcanic field, Utah, Geological Society of America Bulletin 102, 6, 734–748.

424

425 Pullen, A., Ibanez-Mejia, M., Gehrels, G., Giesler, D., Pecha, M., 2018. Optimization of a laser ablation-single

426 collector-inductively coupled plasma-mass spectrometer (Thermo Element 2) for accurate, precise, and efficient

427 zircon U-Th-Pb geochronology. Geochemistry, Geophysics, Geosystems 19, 3689-3705.

428 DOI:10.1029/2018GC007889.

429

430 Rowley, P.D., Anderson, J.J., WIlliams, P., 1975. A Summary of Tertiary Volcanic Stratigraphy of the Southwestern

431 High Plateaus and Adjacent Great Basin, Utah.

432

433   Rowley, P.D., Cunningham, C.G., Steven, T.A., Mehnert, H.H., Naeser, C.W., 1997. Cenozoic Igneous and

434   Tectonic Setting of the Marysvale Volcanic Field and Its Relation to Other Igneous Centers in Utah and Nevada, in:

435   Friedman, J.D., Huffman, C. (Eds.), Laccolith Complexes of Southeastern Utah: Time of Emplacement and Tectonic

436   Setting-Workshop Proceedings, Laccolith Complexes of Southeastern Utah. U.S. Geological Survey Bulletin 2158,

437   pp. 167–201.

438

439   Rowley, P.D., Cunningham, C.G., Steven, T.A., Workman, J.B., Anderson, J.J., Theissen, K.M., 2002. Geologic

440   Map of the Central Marysvale Volcanic Field, Southwestern Utah. Geological Investigations Series I-2645-A.

441

442   Rowley, P.D., Mehnert, H.H., Naeser, C.W., Snee, L.W., Cunningham, C.G., Steven, T.A., Anderson, J.J., Sable,

443   E.G., Anderson, R.E., 1994. Isotopic ages and stratigraphy of Cenozoic rocks of the Marysvale Volcanic Field and

444   adjacent areas, west-central Utah. U.S. Geological Survey Bulletin 2071.

445

446   Sable, E.G., Maldonado, F., 1997. Breccias and megabreccias, Markagunt Plateau, southwestern Utah: Origin, age,

447   and transport directions, United States Geological Survey Bulletin 2153, 151–176.

448

449   Sambridge, M.S., Compston, W., 1994. Mixture modeling of multi-component data sets with application to ion-

450   probe zircon ages. Earth and Planetary Science Letters 128, 373–390, doi:10.1016/0012-821x(94)90157-0.

451

452   Steven, T.A., Cunningham, C.G., Naeser, C.W., Mehner, H., 1977. Revised stratigraphy and radiometric ages of

453   volcanic rocks and mineral deposits in the Marysvale area, west-central Utah, USGS Open File Report 77-569.

454

455   Steven, T.A., Rowley, P.D., Cunningham, C.G., 1984. Calderas of the Marysvale Volcanic Field, west central Utah,

456   Journal of Geophysical Research 89, no. B10, 8751.

457

458   Sundell, K.E., Gehrels, G.E., Pecha, M.E., 2021. Rapid U-Pb geochronology by laser ablation multi-collector.

459   Geostandards and Geoanalytical Research 45, 37-57. DOI:10.1111/ggr.12355.

460

461   Taylor, A.O., Anderson, T.P, O'Toole, W.L., Waddell, G.G., Gray, A.W., Douglas, H., Cherry, C.L., Caywood,

462   R.M., 1951. Geology and Uranium Deposits of Marysvale, Utah, Interim Report on the Producing Area 896,

463   Technical Information Service.

464

465   Vermeesch, P., 2021. On the treatment of discordant detrital zircon U–Pb data. Geochronology 3, 247–257,

466   https://doi.org/10.5194/gchron-3-247-2021, 2021.

467

468   Wender, L.E., Nash, W.P., 1979. Petrology of Oligocene and early Miocene calc-alkalic volcanism in the Marysvale

469   area, Utah: Summary. Geological Society of America Bulletin 90, 2–3. https://doi.org/10.1130/0016-

470   7606(1979)90<2:pooaem>2.0.co;2

471

472   Zamanialavijeh, N., Hosseinzadehsabeti, E., Ferré, E.C., Hacker, D.B., Biedermann, A.R., Biek, R.F., 2021.

473   Kinematics of frictional melts at the base of the world's largest terrestrial landslide: Markagunt gravity slide,

474   southwest Utah, United States. Journal of Structural Geology 153, 104448.

475   https://doi.org/10.1016/j.jsg.2021.104448